Available online at www.sciencedirect.com

SciVerse ScienceDirect

Ceramics International 39 (2013) 1413–1431

CERAMICS INTERNATIONAL

www.elsevier.com/locate/ceramint

Thermal cycling behaviour of plasma sprayed lanthanum zirconate based coatings under concurrent infiltration by a molten glass concoction

C.S. Ramachandran[a,*], V. Balasubramanian[a], P.V. Ananthapadmanabhan[b]

[a]*Centre for Materials Joining & Research (CEMAJOR), Department of Manufacturing Engineering, Annamalai University, Annamalai Nagar 608002, Tamilnadu, India*

[b]*Plasma Spray Technologies Section (PSTS), Laser and Plasma Technology Division (L&PTD), Bhabha Atomic Research Centre (BARC), Anu Shakthi Nagar, Trombay, Mumbai 400085, Maharashtra, India*

Received 7 July 2012; received in revised form 21 July 2012; accepted 24 July 2012
Available online 16 August 2012

Abstract

Thermal barrier coatings (TBCs) used in gas-turbine engines afford higher operating temperatures, resulting in enhanced efficiencies and performance. However, during aero engine operation, environmentally ingested airborne particles, which includes mineral debris, sand dust and volcanic ashes get ingested by the turbine with the intake air. As engine temperatures increase, the finer debris tends to adhere to the coating surface and form calcium magnesium alumino-silicate (CMAS) melts that penetrate the open void spaces in the coating. Upon cooling at the end of an operation cycle, the melt freezes and the infiltrated volume of the coating becomes rigid and starts to spall by losing its ability to accommodate strains arising from the thermal expansion mismatch with the underlying metal. The state-of-the-art ZrO_2-7-weight% Y_2O_3 (YSZ) coatings are susceptible to the aforementioned degradation. Rare-earth zirconates have generated substantial interest as novel thermal barrier coatings (TBC) based primarily on their intrinsically lower thermal conductivity and higher resistance to sintering than YSZ. In addition, the pyrochlore zirconates are stable as single phases at up to their melting point. $La_2Zr_2O_7$ (LZ) is one among such candidates. Hence, the present study focusses on the comparison of cyclic molten CMAS infiltration behaviour of the base metal Inconel 738 (BM), the bond coat NiCrAlY (BC), the duplex YSZ, the LZ coating and a five layered coated specimen with LZ as top layer. Among those coatings mentioned above, the five layer coated specimen showed excellent CMAS infiltration resistance under thermal cycling conditions.

Keywords: B. Failure analysis; D. Glass; D. Spinels; D. ZrO_2

1. Introduction

The Thermal Barrier Coatings (TBCs) are regarded as one of the most successful innovations and applications of coatings in industry. Durability and performance of advanced gas turbines for aircraft propulsion, power generation, marine propulsion and industrial engine applications have been improved with the application of thermal barrier coatings (TBCs) to high pressure turbine (HPT) aerofoils [1]. TBCs are typically deposited via electron beam physical vapour deposition (EB-PVD) or atmospheric plasma spraying (APS). Several million turbine blades and vanes are currently flying. Commercial TBCs are comprised of an oxidation resistant bond coating (typically Pt–Al, NiCrAlY or NiCoCrAlY), a thermally grown oxide (predominately alpha-alumina), and an EB-PVD/APS deposited ceramic coating, which is typically comprised of tetragonal yttria-stabilized zirconia (7–8 wt.% per cent Y_2O_3 stabilized ZrO_2) [2]. With the ever increasing demand to increase the turbine inlet temperature (TIT) for improved engine efficiency, a prime reliant TBC system to effectively protect the hot section turbine components has been a critical requirement for gas

*Corresponding author. Tel.: +91 4144 230382/+91 9843892693; fax: +91 4144 239734/238275.
E-mail addresses: csrcn@rediffmail.com. rcncs@yahoo.com (C.S Ramachandran.).

0272-8842/$ - see front matter © 2012 Elsevier Ltd and Techna Group S.r.l. All rights reserved.
http://dx.doi.org/10.1016/j.ceramint.2012.07.084

turbine engines. Extensive efforts have been made to identify the failure mechanisms of the TBCs to increase the durability and reliability of TBCs [3].

A major disadvantage of the state of the art yttria-stabilized zirconia (YSZ) coating is the limited operation temperature at and above 1200 °C for long-term application. At such higher temperatures, phase transformations from the '**(t′)**'-tetragonal prime to tetragonal and cubic '**(t+c)**' and then to monoclinic '(m)' occur, giving rise to the formation of cracks, leading to the delamination of the coating [4]. An additional concern regarding the degradation of the TBCs apart from the aforementioned phase transformation issue is the presence of siliceous minerals (dust, sand, volcanic ash, runway debris) ingested with the intake air. These contaminants deposit onto the coated surfaces of the components, yielding glassy melts of low melting eutectics in the quaternary CaO–MgO–Al_2O_3–SiO_2 (CMAS) system when the surface temperatures exceed 1200 °C [5]. The problem is more acute in aircraft engines, but there is anecdotal evidence that it also affects industrial and power generation turbines. These aggressive glassy compounds can deposit, melt, and degrade the TBCs via repeated freeze–thaw action and, to a certain extent, direct chemical reaction with TBC constituents. The thermo-mechanical and thermo-chemical interactions can accelerate the failure of TBCs and underlying components by the infiltration of molten deposits into the porous ceramic top coat. This has been frequently reported [6], and it warrants an understanding of the interaction of such molten deposits with the underlying metallic bond coat and base metal. The search for new materials that can withstand higher gas-inlet temperatures (above 1200 °C) has been intensified within the last decade. Lanthanum zirconate ($La_2Zr_2O_7$, LZ) was recently proposed as a promising TBC material. Thermal properties of both bulk LZ material and its coating have been studied [7].

Compared with YSZ, it has a lower thermal conductivity (1.56 $W\,m^{-1}\,K^{-1}$ for LZ, 2.1–2.2 $W\,m^{-1}\,K^{-1}$ for YSZ, bulk materials, 1000 °C) and lower sintering ability. Further LZ maintains single cubic pyrochlore phase from room temperature up to its melting point. It has a low Young's modulus (175 GPa for LZ and 200–220 GPa for YSZ) and the material is oxygen non-transparent compared to YSZ, which makes it an attractive candidate as a TBC material [8]. The present investigation addresses the potential effect of the infiltration of CMAS under thermal cycling condition on the base metal Inconel 738 (BM), the High Velocity Oxy Fuel sprayed NiCrAlY bond coat (BC), the YSZ duplex coating and the LZ duplex coating. In addition, the authors have also attempted to compare the cyclic CMAS attack behaviour of the aforementioned specimens with that of a five layer (with LZ coating as the top layer) coated specimen, since it survived more numbers of thermal cycles at 1280 °C (without CMAS) compared to other coating architectures [9].

2. Experimental work

2.1. Deposition of coatings

An agglomerated and sintered Yttria Stabilized Zirconia (YSZ) spherical powder with the size ranging between 10–45 μm (Make: H.C. Stark, AMPERIT 827.054 powder (ZrO_2, 7 Wt.% Y_2O_3)) was used. Since the Lanthanum Zirconate (LZ) powder is not commercially available, the same was prepared in our laboratory. The method of preparing the plasma spray quality lanthanum zirconate power is available in our previously published paper [10]. The substrate coupons were of nickel based super alloy Inconel 738 material (BM). The chemical composition of the base material (BM) is shown in Table 1.The dimensions of the substrate (BM) coupons were 25.4 × 12.2 × 3 mm. The corners and the edges of the substrate (BM) coupons were chamfered and rounded prior to grit blasting. Grit blasting was carried out using corundum grits of 16 mesh size using an automated high pressure suction blasting system (Make: MEC; India. Model: MEC SUBC MK III) to achieve a roughness average (Ra) of 9–11 μm. The surface roughness was measured using a diamond stylus surface roughness tester (Make: Mitutoyo, Japan; Model: SFTT301). The ceramic powders were plasma sprayed over NiCrAlY (Ni-22Cr-10Al-1Y (wt.%) Make: Praxair NI-343, Size: 10–45 μm) bond coat (BC), which was previously deposited using HVOF (Make: MEC; India. Model: MEC HIPOJET 7100) process on to the grit blasted Inconel 738 coupons (BM). The coatings were made on all the six sides of the grit blasted (BM) coupons. The plasma spray deposition of the YSZ and the synthesized LZ powders were carried out using a semi-automatic 40 kW IGBT-based Plasmatron (Make: Ion Arc Technologies; India. Model: APSS-II). Fig. 1 displays the coatings prepared for CMAS attack test. The various specimen types considered for the investigation are shown in Fig. 1a. The total thickness of all the coatings was kept constant at 500 μm. Since the intermixed layers were involved, the two powder mixtures namely the LZ+YSZ and the YSZ+NiCrAlY powder mixtures (50+50 wt%) were mixed, respectively, in a ball mill (Make: VBCC; India,

Table 1
Chemical composition of the base metal.

Material	Chemical composition												
	Zr	C	Mn	Si	Nb	Ta	Mo	W	Al	Ti	Co	Cr	Ni
Inconel 738	0.1	0.17	0.2	0.3	0.9	1.7	1.7	2.3	3.6	3.4	3.4	16	Bal.

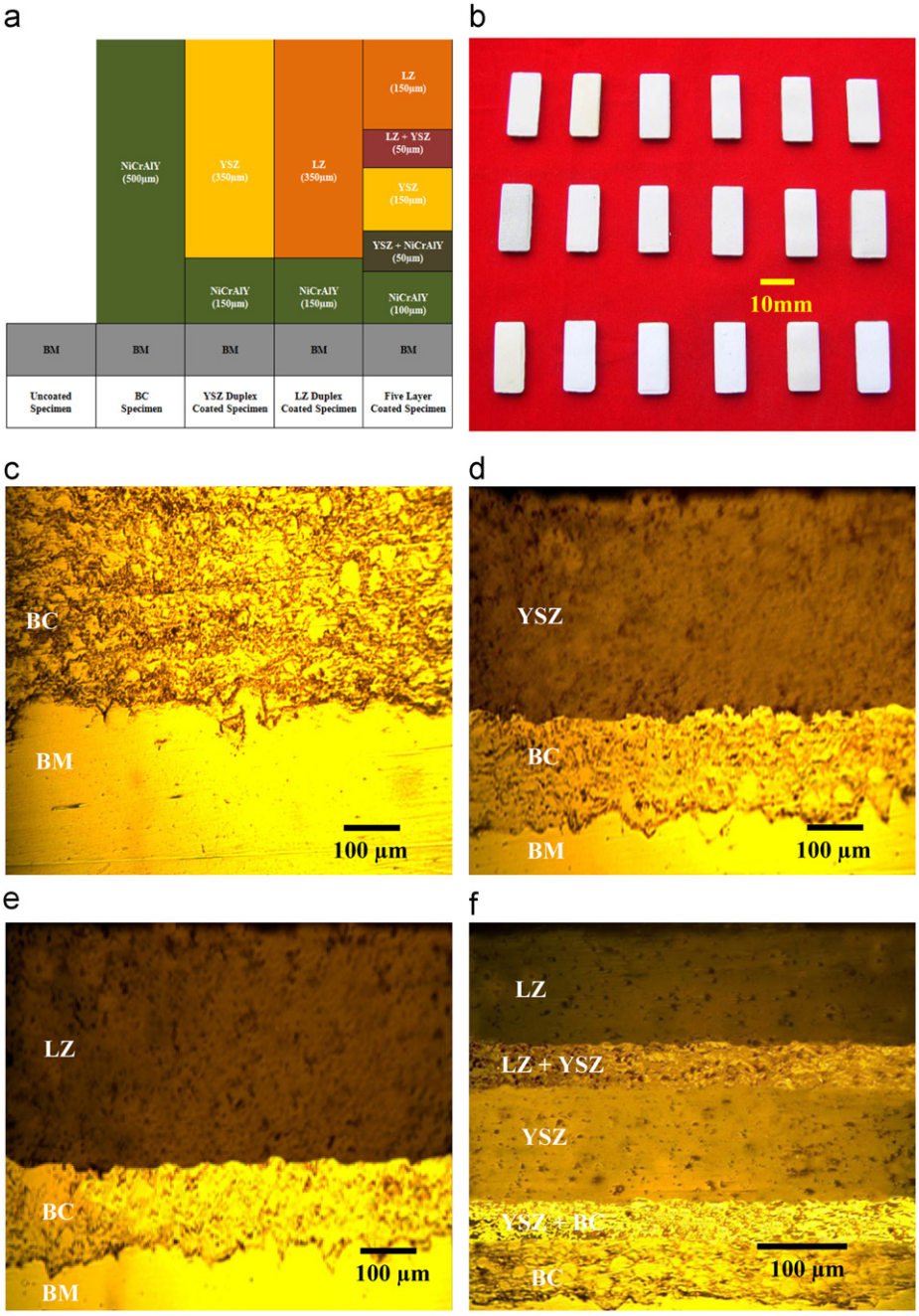

Fig. 1. Coatings prepared for cyclic molten glass infiltration test. (a) Considered specimen architectures, (b) coated coupons for CMAS test, (c) cross section of BC specimen, (d) cross section of YSZ duplex coated specimen, (e) cross section of LZ duplex coated specimen, (f) cross section of five layers coated sample.

Model: HEBM-11) for four hours in dry condition with zirconia balls as the mixing medium prior to deposition. The porosity levels of the ceramic coatings were maintained between 13 and 15 vol.% by appropriately modifying the APS process parameters. The HVOF sprayed BC had a porosity of around 2.0 vol.%. The process parameter settings to deposit the coatings using APS and HVOF spray processes are shown in Table 2. The anode-nozzle diameter of the APS gun was 6 mm. The injection of the powder was carried out inside the anode nozzle right in front of the plasma arc root and perpendicular to the plasma flow direction. The powder carrier gas was Argon having a purity of 99.9%. The powder injector diameter was 2.7 mm and the injector was made out of oxygen free high conductivity (OFHC) copper material. The anode, the cathode, the powder injector and the plasma power supply cables of the APS system are intensively cooled with circulating water having a flow rate of 38 lpm and a temperature of 18 °C. The internal diameter of the HVOF gun's throat was 12 mm. The powder was injected into the HVOF gun coaxially. The HVOF gun houses a 3.2 mm orifice controlled powder injector made out of 316 LN

Table 2
Process factors and their respective levels.

APS/ HVOF factors	YSZ (APS)	LZ (APS)	NiCrAlY (HVOF)
Power (kW)	26	24	–
Stand-off distance (mm)	115	115	210
Primary/secondary gas flow rate (APS: Ar/N_2, HVOF: Air/Butane/O_2) (lpm)	38/5	38/4	950/80/250
Powder feed rate (gpm)	21	21	38
Carrier gas flow rate (APS: Ar, HVOF: Moisture free air) (lpm)	11	9	12

stainless steel material. The 250 lpm of moisture free compressed air supplied into the HVOF gun takes care of the cooling requirements satisfactorily. The deposited coatings as such are shown in Fig. 1b.

2.2. Characterization and mechanical properties evaluation of coatings

The coated specimens were sectioned using a slow speed metallurgical sample saw (Make: Ducom, India; Model: MSS-10) equipped with resin bonded diamond cutting disc. Customary metallographic procedures were adopted to polish the cross-section of the coatings. The cross-sectional images of the specimens were captured using optical microscope (Make: Meiji; Japan. Model: MIL-7100). The porosity was analyzed as per ASTM: B276 standard on the polished cross section of the coating using the same optical microscope equipped with image analyzing system. A 100 μm square area was selected on the polished cross section of the coating and the image was analyzed. The same procedure was repeated at five random locations to find out the average percentage volume of porosity. The microhardness measurements were made on the polished cross-sections of the coatings, using a Vickers microhardness tester (Make: Shimadzu; Japan. Model: HMV-2T). A load of 2.94 N and a dwell time of 15 s were used to evaluate the hardness. Hardness values were measured at 10 random locations on the polished cross-section of a coating. The tensile bond strength test was carried out as per ASTM: C633 standard using a universal testing machine (Make: FIE Blue Star; India. Model: UNITEK-94100). A commercially available heat curable epoxy was used as an adhesive, to test the coated specimens. The method of conducting the bond strength test and the analysis thereof can be referred in our previously published paper [11]. The coatings were also subjected to SEM and EDAX analysis (Make: Quanta; Switzerland. Model: 3D FEG-I). The coatings were also analyzed using X Ray Diffraction (Make: Rigaku, Japan; Model: ULTIMA-III).

2.3. Cyclic CMAS infiltration test method

The cyclic CMAS attack test was carried out, using a 1800 °C tubular sintering furnace (Make: VBCC; India, Model: VBHTSF-1800MF12). For cyclic CMAS infiltration tests, a composition of $33CaO–9MgO–13Al_2O_3–45SiO_2$ was selected [12]. The compositions are given on weight percentage basis. The CMAS ingredients were mixed in a ball mill for four hours with suitable amounts of demineralized water and corundum balls as mixing medium. The mixed ingredients were placed in a Pt–Rh crucible and melted in a furnace at 1550 °C for four hours. To ensure homogeneity, the resulting glass was crushed and then remelted using the same conditions as the first melting. The remelted CMAS glass was then crushed again in a ball mill in dry condition with corundum balls, and the consequential frit was screened using a #500 mesh sieve. The CMAS glass thus prepared was used on the specimens for the cyclic CMAS attack test. Prior to applying the CMAS concoction, the specimens were pre-heated at 250 °C for one hour, as preheating provided good adhesion of CMAS to the specimen. The CMAS frit was mixed with ethanol using an agate mortar and pestle to form slurry. The CMAS slurry concoction was spread over the top surfaces of the preheated specimens using a glass fibre brush. The CMAS concentration was kept in the range of 34–36 mg/cm^2 leaving a 3 mm distance from the edges (without CMAS spreading) to avoid edge effect. These CMAS containing specimens were dried in the furnace at 250 °C for one hour to remove the moisture from the CMAS deposit.

Post drying, the CMAS covered specimens were placed on recrystallized alumina crucibles and inserted directly into the hot zone having a temperature of 1280 °C. In this hot zone the specimens were exposed to the aforesaid temperature for 50 minutes (the CMAS mixture was molten on the specimen surface during the exposure). This was followed by cooling the coupons for 10 minutes under a diffused air cooling arrangement leading to room temperature. This one hour cycle was repeated for 50 times (50 cycles). Further, during cyclic CMAS exposure, the weight differences of the coatings were measured once in every two cycles. The weight of crucibles and the specimens were measured together by means of a precision weighing machine (Make: Shimadzu; Japan. Model: AW 320) with 0.01 mg of resolution to determine the specific weight gain of the specimens. The spalled scales of the specimens were also included at the time of the measurements of weight change to determine the specific weight gains of the specimens. The samples were not supplemented with additional CMAS concoction during cycling.

3. Results

The cross-sectional micrographs of the coatings before cyclic CMAS attack test are presented in Fig. 1c–f. The cross-sectional micrograph of the BC is shown in Fig. 1c which display well packed dense lamellar structure. The duplex YSZ and LZ coatings (Fig. 1d and e) display a sharp and clear interface between the ceramic coat and the BC. The LZ–YSZ coating interface and the YSZ–BC interface of the five layered coating do not exhibit a clear interface (Fig. 1f) due to the presence of the 50 μm thick

intermixed interfacial layers. The evaluated mechanical properties of the coatings represented in graphical format with error bars are shown in Fig. 2. The hardness distribution of the LZ, YSZ and the five layered coatings are shown in Fig. 2a. An average microhardness value of 954 $HV_{0.3}$ was recorded in the case of LZ coating and an average hardness value of 907 $HV_{0.3}$ was recorded in the case of YSZ coating. The average hardness values of the LZ–YSZ interface layer and the YSZ–BC interlayer of the five layered coating were 932 and 625 $HV_{0.3}$ respectively. The tensile bond strengths of the LZ, YSZ and the five layered coatings are shown in Fig. 2b. A tensile bond strength value of 12 MPa was recorded in the case of the LZ duplex coating; 15 and 20 MPa were the bond strengths of the YSZ duplex and the five layered coatings, respectively. The weight gain details of the coatings after CMAS test are shown in Fig. 3. The specific weight gains of the coatings and the BM, due to cyclic CMAS attack are shown in Fig. 3a. From the figure it can be said that all the coatings and the BM do not exhibit a parabolic weight gain pattern. The cumulative weight gains of the coatings and the BM are shown in Fig. 3b. The highest weight gain of 26 mg/cm^2 was recorded in the case of the BM. A cumulative weight gain of 19, 9, 14 and 6 mg/cm^2 were recorded in the case of the BC, YSZ, LZ and the five layered coated specimens, respectively.

4. Discussion

4.1. Interaction between CMAS and base metal (BM) Inconel 738

The cumulative weight gain of the BM is 26 mg/cm^2 (Fig. 3b). The measured weight gain is a combination of infiltration, oxidation along with the infiltration process when the metallic phases transform into the ceramic phases and the transformation between the ceramic phases formed.

4.1.1. Surface analysis of BM after CMAS attack

The SEM image of the BM exposed to 50 CMAS attack cycles is shown in Fig. 4. The observation of the surface of the BM showed that the oxide scales of the BM spalled

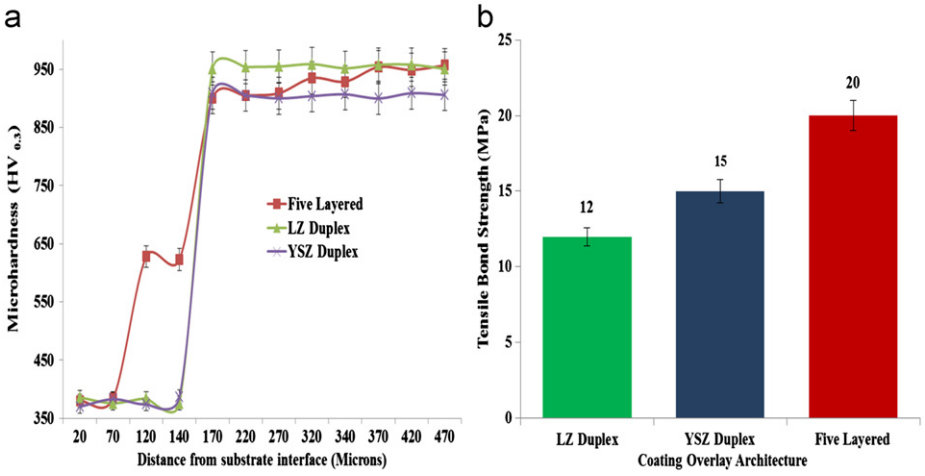

Fig. 2. Mechanical properties of the coatings. (a) Microhardness distribution in coatings, (b) Tensile bond strength of coatings

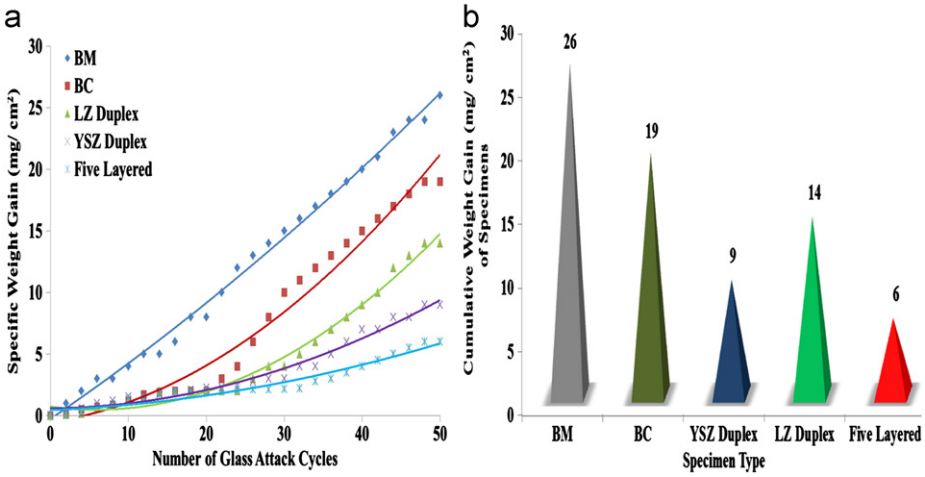

Fig. 3. Weight gain of the coatings after the cyclic CMAS test. (a) Specific weight gain of coatings with respect to number of CMAS attack cycles, (b) Cumulative weight gain of specimens up to 50 CMAS attack cycles

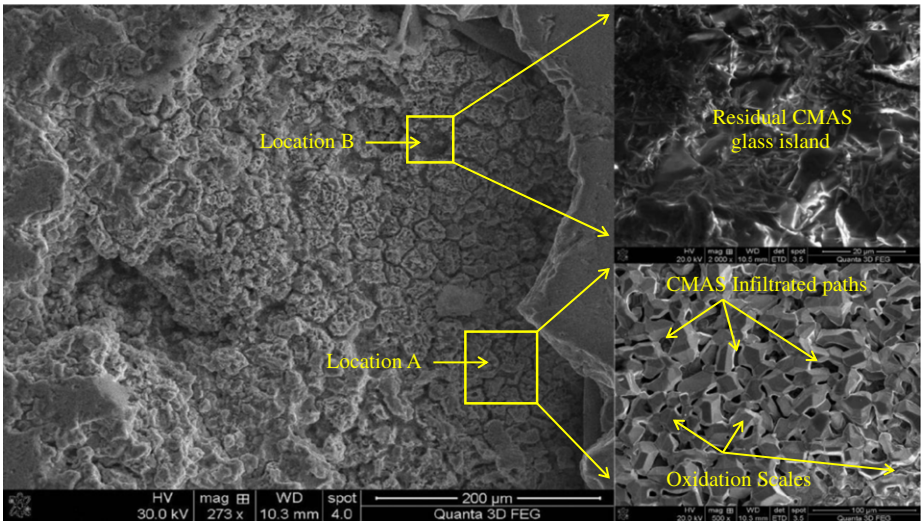

Fig. 4. SEM image of top surface of BM exposed to CMAS indicating oxide scale formation, CMAS infiltrated paths and residual CMAS glass island.

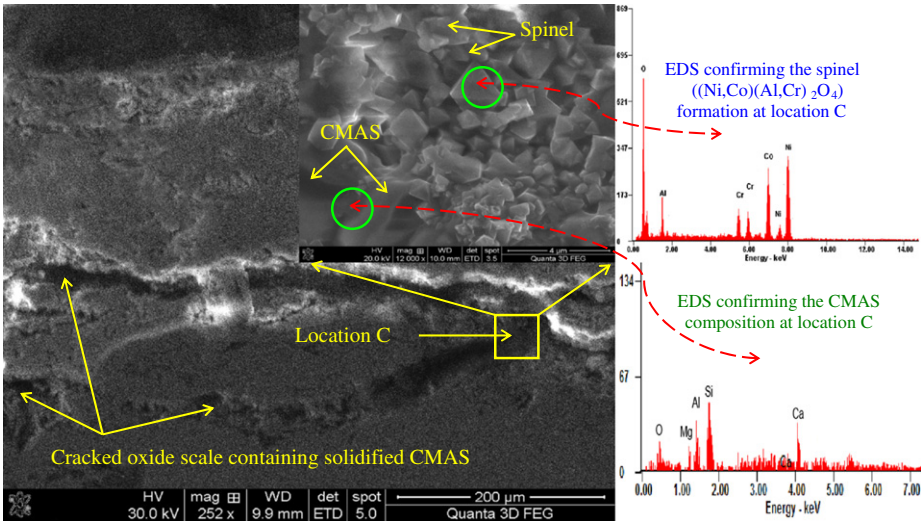

Fig. 5. Cross-sectional image of BM sample exposed to CMAS showing the cracked oxide scale containing the spinel and the solidified CMAS.

rigorously after the 50-hour cyclic CMAS attack test as seen in Fig. 4. The surface of the BM also exhibits two different morphologies, indicated as location A and location B in Fig. 4. Location A in Fig. 4 indicates that the molten CMAS has attacked the grain boundaries of the BM and penetrated through it. Since grain boundaries are energy rich regions, the low viscous glass preferentially attacks the grain boundaries, leaving behind lots of entry holes/infiltration paths. The grains were not left unaffected. Severe oxidation of the grains has taken place and a thick oxide scale was found on the surface. There were some isolated regions where the un-infiltrated CAMS glass could be seen on the surface of the BM as seen in Location B in Fig. 4. It can be observed in Fig. 3a that there is an increase in the weight with the increase in the number of the CMAS attack cycles. The increase in specific weight gain may be attributed to the higher fluidity of the CMAS concoction. The highly fluidic CMAS acts as an oxygen carrier leading to a combined increase in the diffusion and transport phenomenon. The protective scale is destroyed or eliminated by molten CMAS and consequently the metal surface is exposed to the direct action of the destructive environment. The molten CMAS also provides rapid diffusion paths for reactant species which lead to the cracking and exfoliation of the protective scale. The cracks may have allowed the aggressive liquid CMAS glass to reach the virgin metal surface, contributing to the continuation of exfoliation of the oxidized BM scales, till the end of the test.

4.1.2. *Cross-sectional analysis of BM after CMAS attack*

The cross-sectional morphology of the BM after 50 cycles of CMAS attack is shown in Fig. 5. From the figure, one could see that the thickness of the CMAS infiltrated zone is almost 350 µm thick and is characterized by oxide scale with large cracks running parallel to the surface of the BM. One can see the presence of solidified CMAS inside those cracks. Upon closer inspection of the glass

solidified inside the cracks (Location C in Fig. 5), it was observed that the molten CMAS has reacted with the BM, leading to the formation of spinels. Islands of unreacted CMAS were also found along with the spinel. The crystal structure of the spinel exhibits, almost regular hexagons, and some rectangular crystals. The glass islands were analyzed using EDS and the CMAS composition was confirmed (Fig. 5). The EDS analysis of the crystallized spinel is shown in Fig. 5. The EDS analysis matches with that of the spinel having the composition (Ni,Co) $(Al,Cr)_2O_4$. The surface oxides of the BM specimen are more porous and coarse. A series of chemical reactions that can take place during the cyclic CMAS attack on the BM are elucidated in the following section.

The chromium and the aluminium have more affinity towards oxygen; hence they form in the initial stages of CMAS attack

$$2Cr + 3/2O_2 \rightarrow Cr_2O_3 \quad (1)$$

$$2Al + 3/2O_2 \rightarrow Al_2O_3 \quad (2)$$

The Nickel will also participate in the oxidation process

$$Ni + 1/2O_2 \rightarrow NiO \quad (3)$$

The formations of Al_2O_3 and Cr_2O_3 on the surface are beneficial for oxidation resistance, but these oxide scales were not continuous and hence permitted the transportation oxide species. This oxide transport enables the formation of spinels, as mentioned below

$$NiO + Cr_2O_3 \rightarrow NiCr_2O_4 \quad (4)$$

$$NiO + Al_2O_3 \rightarrow NiAl_2O_4 \quad (5)$$

Cobalt also undergoes the same kinds of reactions to form spinels. The aforementioned reactions, the SEM and the EDS analysis confirm the formation of complex oxides on the BM surface. The formation of these complex oxides imposes a severe strain on the oxidized scale [13]. Such a kind of severe strain may result in the cracking and spallation of the oxide scale, exposing the virgin BM to the aggressive molten CMAS concoction. This tendency of the spalling has also been explained as a result of the predominance of cationic diffusion in the growth of scales where no oxide is formed at or near the external surface. Voids and porosity gradually develop at or near the metal scale interface due to the reduced volume of metal and lack of sufficient plastic deformation of scale [14]. This leads to a reduction in adherence as well as coherency of the scale, thereby increasing the tendency of spalling.

4.2. Interaction between CMAS and NiCrAlY bond coat (BC)

The specific weight gain pattern of the NiCrAlY BC exposed to 50 cycles of CMAS attack is shown in Fig. 3a. The cumulative weight gain of the BC is 19 mg/cm^2 (Fig. 3b). The specific weight gain pattern and the cumulative weight gain value indicate that the BC has provided sufficient protection to the BM from the molten CMAS attack.

4.2.1. Surface analysis of BC after CMAS attack

For the BC, the surface structure comprised of a combination of crystallized glass, oxidized splats, CMAS infiltration paths, ridges and nodules (Fig. 6). The whiskers and nodules are usually deemed as characteristic features for growing Al_2O_3 [15], which can be seen as residues of outward growth, due to cation lattice and surface diffusion, as seen in Location D in Fig. 6. The formation of Al_2O_3 was confirmed using the EDS analysis, which is shown in Fig. 6. On the surface of BC, spallation of alumina scale occurred as well. It is well known that NiCrAlY coatings protect the substrate superalloy against oxidation, by forming a protective oxide scale [16]. In this

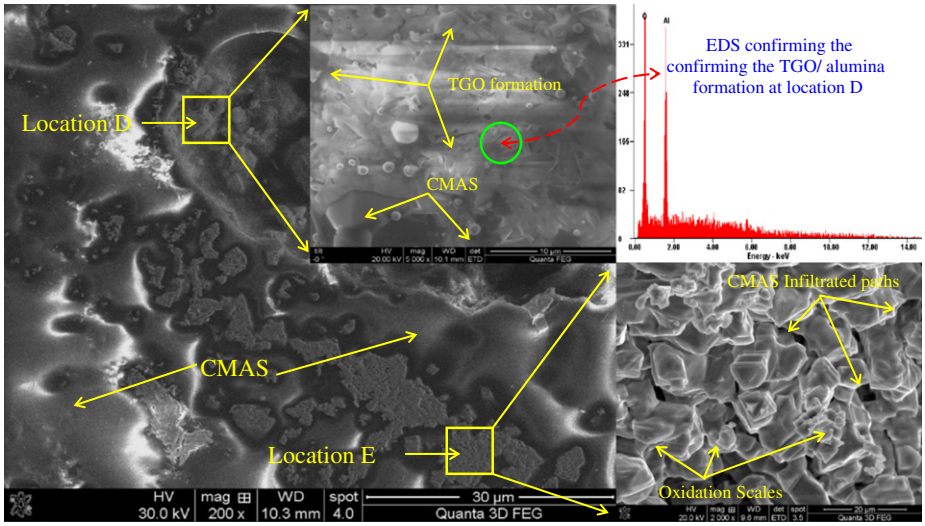

Fig. 6. SEM image of top surface of BC exposed to CMAS indicating TGO formation, CMAS infiltrated paths and oxide scale formation.

study, the protective oxide scale formed on the coating was mainly Al_2O_3 scale, which could act as a barrier and shield the coating to a certain extent, from the incursion of liquid CMAS concoction. The depletion of Al from the coating is considered as a key factor in assessing the service life of NiCrAlY coating, at high temperature. During the high temperature cyclic CMAS exposure, the loss of Al by inward and outward diffusion must be considered simultaneously. Due to the combination of oxidation and interdiffusion, the Al content decreases and correspondingly leads to the alternation of coating structure. Here, the NiCrAlY coating degraded rapidly at high temperature and showed a limited capability in self-healing. During the high temperature cyclic CMAS attack, the protective Al_2O_3 scale would be consumed in two ways. One is that the stress caused by the thermal cycling will lead to possible crack or spallation of Al_2O_3 scale. Another is the reactions with CMAS concoction might result in the dissolution of the Al_2O_3. As the CMAS infiltration proceeds, Al reservoir in the coatings will be consumed to repair the Al_2O_3 until being exhausted. Once the Al_2O_3 scale cannot be maintained, the molten CMAS would react directly with the coatings and lead to the ultimate failure. The molten CMAS concoction, which was deposited on the superalloy, can flux and dissolve the normally protective oxides such as Cr_2O_3 and Al_2O_3. The surface also exhibits number of CMAS infiltration paths as seen in Location E in Fig. 6 which is suggestive of the penetration of molten CMAS along the splat boundaries.

4.2.2. Cross-sectional analysis of BC after CMAS attack

The cross-section of the BC sample is shown in Fig. 7. The CMAS attacked BC surface also exhibits scale formation to a thickness of around 180 μm as seen in Fig. 7. The figure shows that due to the selective oxidation of chromium and aluminium, Cr_2O_3 and Al_2O_3 are formed along the boundaries of nickel-rich splats, and in pores and blocked the passages and thus enabled the BC to develop a temporary barrier against the penetration and diffusion of liquid CMAS. Additionally, very low porosity and the flat splat structure of the coatings have also contributed in developing resistance to CMAS penetration at higher temperatures, since the molten glass mostly propagate along the splat boundaries and through the pores and voids. Due to the dense and flat splat structure of the coatings, the distance from the coating surface to the coating-substrate interface along splat boundaries, is highly increased, which enables the coatings to develop resistance to CMAS infiltration.

The formation of thick oxide layers in the scale, have contributed to the better CMAS infiltration resistance of BC, compared to the BM. Though the Cr_2O_3 and the Al_2O_3 have acted as barriers, the penetration of the aggressive liquid CMAS concoction into the BC has not been completely eliminated. Location F in Fig. 7, on the other hand, displays the evidence of the presence of crystallized CMAS and the formation of the spinel. The formation spinel phase (thin elongated platelets) could be due to the dissolution of Al and Ni by the molten CMAS concoction, developing into the generation of porous mixed oxides. From the EDS elemental analysis shown in Fig. 7, it could be said that this fluxing mechanism is responsible for disassociating the protective alumina layer and the formation of nickel oxide (NiO) and porous spinel $(Ni)(Al,Cr)_2O_4$. In this way, the penetration of molecular oxygen and the molten CMAS along splat boundaries, is allowed in the BC, thereby promoting its oxidation and crack formation tendency. The molten CMAS consumed the thermally grown oxide (TGO), alpha-Al_2O_3 during the test as shown in Fig. 7.

By conducting the EDS analysis (Fig. 7), on the crystallized CMAS, it was found that the composition is rich in Al content, which confirmed the dissolution of the TGO, alpha-Al_2O_3. Crystallization of CMAS glass through enrichment of Al content has been reported earlier [17], where anorthite, $CaAl_2Si_2O_8$ (CMAS glass composition

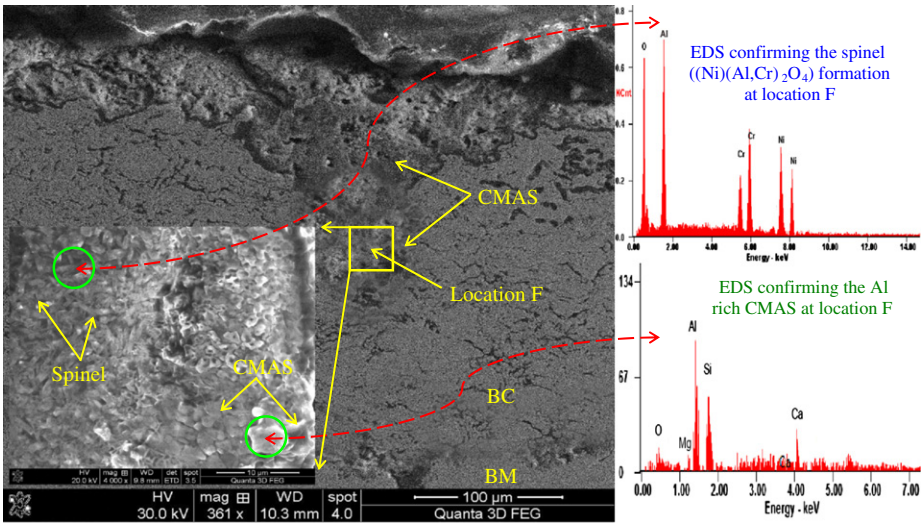

Fig. 7. Cross-sectional image of BC sample exposed to CMAS indicating CMAS infiltrated zone containing spinel and Al rich CMAS.

which is easier-to-crystallize) was found to be the predominant crystallite. The spalled scales of the BC were crushed and were exposed to the XRD analysis. From the XRD pattern (Fig. 8) it could be inferred that the hexagonal anorthite and the cubic spinel were the major phases and nickel oxide and orthogonal magnesium aluminate were the minor phases. Based on CaO-SiO_2-Al_2O_3 ternary phase diagram [18], typical CMAS glass composition without considering the Mg content, falls in pseudo-wollastonite field, whose glass composition is difficult to crystallize. Enrichment of Al content in CMAS shifts this "difficult-to-crystallize" pseudo-wollastonite glass composition to a "crystallizable" Al-rich glass composition that falls in the anorthite field. Thus the dissolution of alpha-Al_2O_3 by CMAS resulted in crystallization of CMAS to anorthite ($CaAl_2Si_2O_8$) phase. Concurrently, the localized enrichment of Mg content promoted the formation of $MgAl_2O_4$ spinel. The formation of anorthite phase improved the CMAS infiltration resistance of the BC to a certain extent, which resulted in the low weight gain compared to BM. The spallation of BC was also observed during the test, which may have resulted due to the rapid growth of void-like defects lying adjacent to coating protuberances, where the tensile radial stress (stress developed during cooling as a result of the thermal contraction) mismatch between the oxide scale and the coating is maximum. The formation of cracks in the coating usually originates from stresses developed in the oxide scale-BC interface.

4.3. Interaction between CMAS and YSZ duplex coated samples

The cumulative weight gain of YSZ duplex coated specimen is 9 mg/cm^2 (Fig. 3b). The aforementioned value and the specific weight gain pattern for 50 CMAS attack cycles (Fig. 3a) indicate the superior CMAS infiltration resistance of YSZ coating compared to BM and BC.

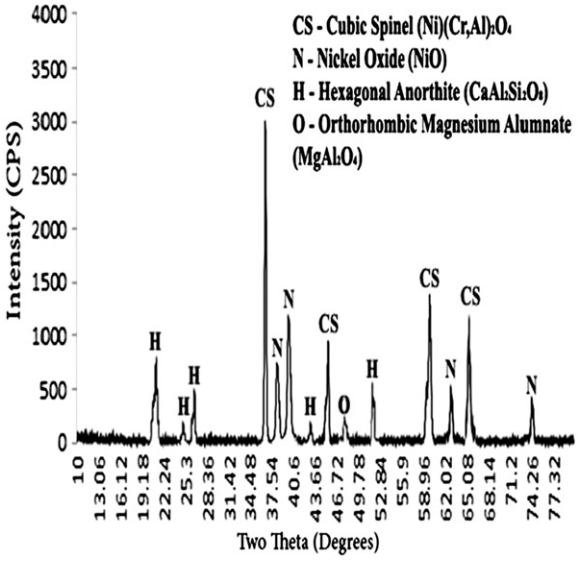

Fig. 8. XRD analysis of crushed BC scale after 50 CMAS attack cycles.

4.3.1. Surface analysis of YSZ duplex coated samples after CMAS attack

The top surface microstructure of the YSZ duplex coating exposed to CMAS attack is shown in Fig. 9. The surface exhibits exfoliated coating lamellae through which the CMAS has infiltrated. The CMAS attack on thermally sprayed YSZ coatings is very aggressive due to the splat-layered structure of the coating. The CMAS dissolves the coating lamellae by attacking the micro-cracks and splat boundaries first. Fig. 9 also displays the presence of spallation cracks on the coating surface. These cracks might be associated with the presence of CMAS deposit and coating densification. Severe frothing was observed during the initial stages of the test. The frothing reaction generates new kind of porosities. The surface deposits appear to have been in a liquid state with sufficient gas content to cause frothing. Frothing of molten glass can occur when calcia and silica are present among the components. But the cause of the frothing phenomenon is still under debate.

4.3.2. Cross-sectional analysis of YSZ duplex coated samples after CMAS attack

The cross-sectional micrograph of the YSZ duplex coated sample is shown in Fig. 10. There are lots of pores, voids and cracks present throughout the cross-section of the coating and these cavities and cracks have been filled with crystallized glass. It has been reported that the CMAS composition starts to melt at approximately 1235 °C when made from the constituent oxides. It is completely molten at 1250 °C and it can infiltrate the pores and cracks present in the coating. Further, the possible reason behind the

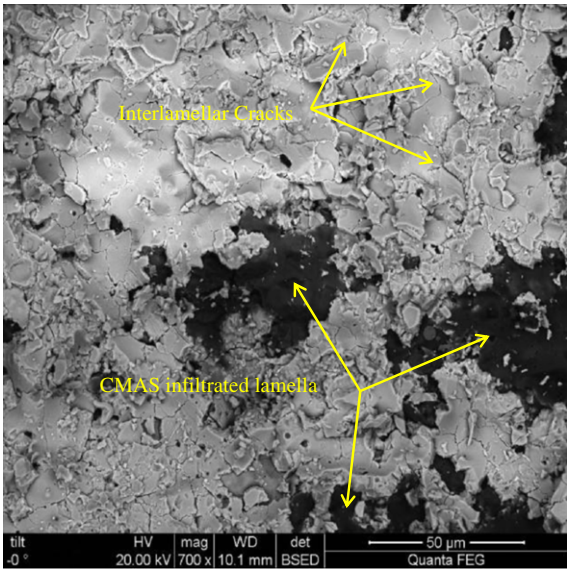

Fig. 9. SEM image of top surface of YSZ duplex coated sample exposed to CMAS.

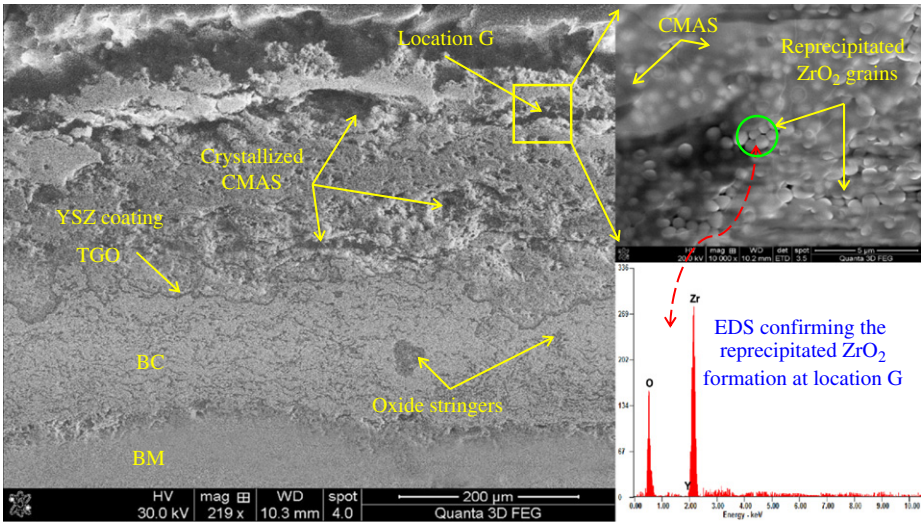

Fig. 10. Cross-sectional image of YSZ duplex coating sample exposed to CMAS indicating CMAS infiltration and reprecipitated spherical shaped ZrO_2 grain formation.

formation of voids and pores is that the air within the porous coating structure tries to escape from it and is trapped within the solidified CMAS infiltrated coating layer. The large voids could also be produced due to some reactions that produce gases, when the TBC is severely attacked by CMAS which can be seen in Fig. 10. The coating failure observed in this study involves the spallation of the top layer coating which has been infiltrated with the CMAS. The incipience of the CMAS attack seems to involve physical damages.

The CMAS attack on YSZ duplex coated specimens also involves the following thermo-chemical mechanisms:

1. The molten CMAS glass wets YSZ and infiltrates into pores and cracks in the TBCs.
2. YSZ grains dissolve in the molten CMAS glass and then reprecipitate as globular grains that are depleted in Y solute. A higher magnification SEM image taken at location G displays (Fig. 10) globular ZrO_2 grains along with crystallized CMAS. Globular nature of the ZrO_2 grains in the glassy matrix provides a strong indication for diffusion-controlled dissolution–reprecipitation [19]; the transformation of t′-ZrO_2 to m-ZrO_2 appears to have taken place during that dissolution–reprecipitation. The EDS (Fig. 10) analysis performed on the globular grains taken at location G confirms that those are ZrO_2 grains.
3. The Zr and Y elements incorporated in the CMAS glass have little or no effect on the glass behaviour.
4. CMAS glass penetrates YSZ grain boundaries, resulting in the energetically favourable dispersion of exfoliated YSZ grains in glass. i.e., one ZrO_2/ZrO_2 grain boundary and two ZrO_2/glass interfaces. This phenomenon has been observed in dense, polycrystalline Al_2O_3 and Si_3N_4 in contact with molten glasses. However, in those cases the dispersed Al_2O_3 and Si_3N_4 grains are generally faceted [20].
5. Possible diffusion of Y from YSZ grains to the CMAS glass occurs, in conjunction with counter-diffusion of Al, Si, Ca, and Mg from the CMAS glass into YSZ grains [21].

The phases present in the YSZ coatings before and after CMAS exposure are displayed in Fig. 11. The XRD plot of the as sprayed YSZ duplex coating shown in Fig. 11a displays the presence of t′ (tetragonal prime) phase which generally occurs due to the rapid quenching of the APS sprayed YSZ splats, whereas the XRD pattern of the CMAS infiltrated YSZ coating (Fig. 11b), shows the presence of t (tetragonal), m (monoclinic) and c (cubic) phases of ZrO_2 along with anorthite and orthorhombic magnesium aluminate/magnesia spinel. The Interaction between the YSZ and CMAS was observed to occur starting at 1250 °C, where CMAS was found to melt and infiltrate the porous YSZ coating. CMAS melt in the YSZ resulted in the dissolution of the YSZ followed by the reprecipitation of ZrO_2 grains with different polymorphs and composition based on the local melt chemistry. The disruptive phase transformation of t′ to t+m and t to m+c occurred. This phase transformation to Y_2O_3-poor monoclinic ZrO_2 (m) and Y_2O_3-rich cubic ZrO_2 (c) phases is attributed to the deviation in the content of Y_2O_3 stabilizer from the original YSZ solid solution during reprecipitation [22]. The YSZ coating exposed to the CMAS melt was found to undergo the disruptive phase transformation to m-ZrO_2 significantly, with some amount of cubic (c) ZrO_2. This could be due to an increase in Y content in CMAS during simultaneous dissolution of YSZ and ingression of CMAS melt through the thickness of the YSZ coating. Thus, reprecipitation of Y_2O_3-depleted monoclinic ZrO_2 and consequently increased the Y content in the CMAS melt and forced the reprecipitation of

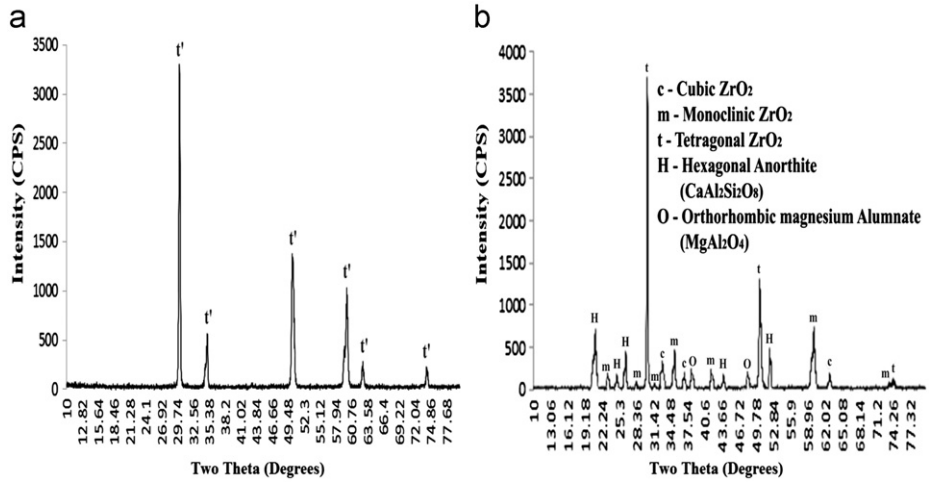

Fig. 11. XRD patterns of YSZ coating before and after CMAS test. (a) XRD pattern of as deposited YSZ duplex coating. (b) XRD analysis of crushed YSZ coat (spalled) after 50 cycles of CMAS attack

Y_2O_3-rich cubic ZrO_2 phase. Further, the presence of c-phase of ZrO_2 in the CMAS attacked YSZ coating is an indication, that the Ca atoms have diffused into YSZ and increased the stability of c-YSZ.

The incorporation of calcium into the YSZ layer can lead to an increase of YSZ volume and a change in stress distribution within the whole TBC system [23]. Upon thermal cycling, this can lead to crack nucleation and their further growth at the YSZ/BC interface. This failure mechanism can be witnessed in Fig. 10, where the inner surface of the YSZ layer was significantly decomposed and infiltrated by the CMAS. It is a known fact that, too much phase transformation of (t–m) ZrO_2 would cause large volume expansion and deteriorate the integrity of TBC system, and eventually spallation failure of TBC. On the other hand, the CMAS led to an accelerated sintering of YSZ coating. Sintering usually leads to shrinkage at the surface of a TBC. The sintering effect decreases gradually from the surface to the bond coat. This leads to an increase in Young's modulus which decreases strain tolerance capability of the coating and increases top-coat stresses [24]. The thermal diffusivity of the YSZ coating with CMAS infiltration will be higher than that of the coating without CMAS infiltration. The sintering will also increase the thermal diffusivity [25]. Therefore, it can be established that the CMAS penetration could compromise the thermal barrier capability of TBC. As a result, the cooling effectiveness could be decreased and cause local over-heating of the BM and BC. Simultaneously, due to degradation of thermal barrier effects, the temperature at the interface between the YSZ top coat and the BC will rise up accordingly. Accelerated thickening of thermally grown oxide (TGO) could occur, which would lead to premature spallation of TBC lamellae. The SEM micrograph shown in Fig. 10 also displays phase assemblage of the TGO layer consisted of alpha-alumina. While most sections of the TGO layer which appeared dense and homogeneous, some regions revealed a high defect density characterized by clustered porosity and numerous microcracks. These microcracks in the TGO layer provided a convenient path for further diffusion of CMAS constituents through the TGO layer to the TGO/bond coat interface.

The variation in the stress distribution also changes the strain energy release rate and failure mechanisms. This may be the mechanism by which the horizontal cracks form and the TBCs spall. The weight gain of these ceramic coated samples is due to the TGO formation and the high internal oxidation of the BC and the BM. The EDS elemental mapping results of the YSZ duplex coating exposed to 50 cyclic CMAS exposures is shown in Fig. 12. From Fig. 12 it could be seen that at the very top, a thin film of unpenetrated CMAS still remains. The dark areas are pores and voids. It can be seen clearly that the YSZ coating is almost destroyed, with the CMAS glass reaching to the bottom of the top coat through the cracks and inter connected porosities. Fig. 12 shows corresponding Ca, Mg, Al and Si EDS elemental maps, respectively, and thus bears an evidence of CMAS reaching the bottom of the TBC. The molten glass wets the YSZ coating and infiltrates into the pores and vertical cracks in the TBC. Simultaneously, the ZrO_2 grains dissolve in the molten CMAS glass and then reprecipitate in globular forms. It is possible that these, and alternative, mechanisms are active in this investigation. The silica has a significant influence on the sintering behaviour of YSZ coating, promoting sintering of the coating during high-temperature annealing. The silica glass has a low viscosity at elevated temperatures and can promote densification by liquid-phase sintering [26]. It has been shown by researchers that SiO_2 was detrimental to the thermal cyclic life times of YSZ coating. In zirconia ceramics, SiO_2 was segregated at grain boundaries and enriched in triple points. Y_2O_3 was precipitated from YSZ grain boundaries, which led to local instability. Otherwise, SiO_2 caused the ZrO_2 to undergo super-plasticity and accelerated the sintering speed [27]. It can be supposed that for the TBC with deep CMAS

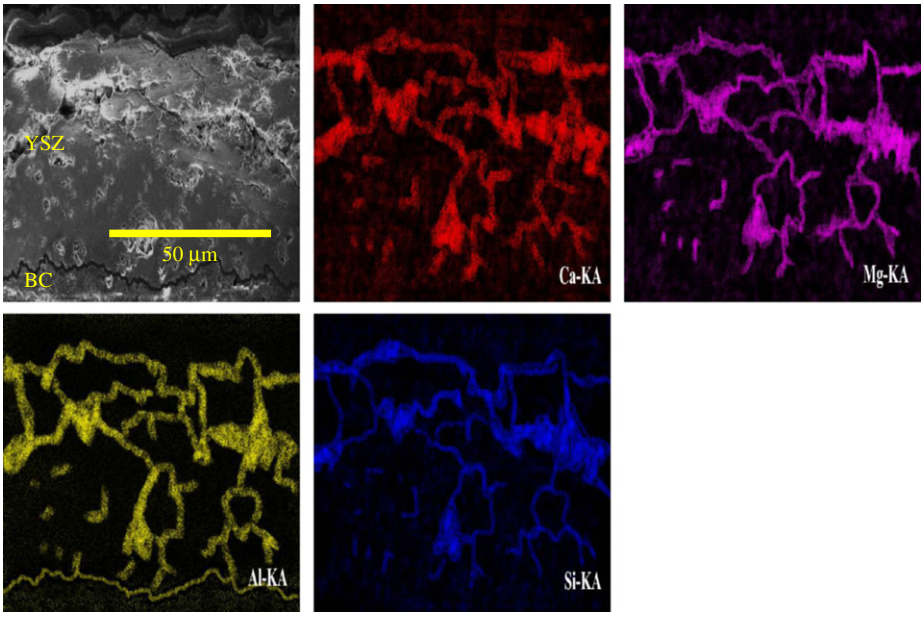

Fig. 12. EDS elemental mapping results of YSZ duplex sample exposed to CMAS attack.

penetration, the thermal barrier function would be severely compromised.

4.4. Interaction between CMAS and LZ duplex coated samples

The specific weight gain pattern of the LZ coating is shown in Fig. 3a. In the figure one can see that the specific weight gain of LZ coating is less compared to YSZ duplex coated specimen up to 23 cycles, but after 23 cycles the weight gain is high, compared to YSZ duplex coated sample. The cumulative weight gain (Fig. 3b) of LZ duplex coated sample is 14 mg/cm^2 and this weight gain value is higher than that of the value recorded for YSZ duplex coating.

4.4.1. Surface analysis of LZ duplex coated samples after CMAS attack

The top surface morphology of hot corroded LZ duplex specimen is shown in Fig. 13. From the figure it can be seen that the LZ duplex coating has experienced severe cracking and delamination during the CMAS attack test. These cracks can further contribute to the deterioration of the coating. In the same figure, one can see that the CMAS has penetrated and exfoliated the LZ coating lamellae (Fig. 13). To establish a self-consistent thermo-mechanical interpretation of the cracking and delamination phenomena evident in the CMAS penetrated zone, three aspects of the mechanics must be rationalized [28]: (i) The temperatures and thermally induced stresses. (ii) Channel cracking at the surface and the penetration of these cracks into the CMAS-penetrated TBC. (iii) Delamination in the TBC at various levels beneath the surface. The cooling scenario envisages the TBC being on a thick, actively cooled substrate. In this investigation, the

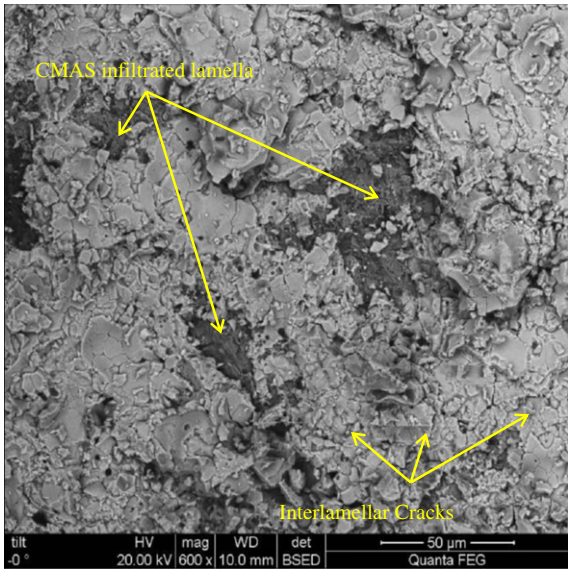

Fig. 13. SEM image of top surface of LZ duplex coated sample exposed to CMAS.

TBC has been at the high temperature for a sufficiently long period so that any stresses fully relax by creep. Moreover, cooling is sufficiently rapid so that the response throughout the surface must be thermo-elastic. The basic context of the CMAS penetrated coating under cyclic thermal loading as per the aforementioned phenomenon is as follows: Upon cooling to ambient temperature from 1280 °C the CMAS solidifies, the penetrated layer develops composite thermo-mechanical properties comparable to that of dense LZ coating.

Once the CMAS solidifies, the high in-plane stiffness causes large, near-surface, tensile stresses. The ensuing stress state is comparable to that associated with a thin film in

residual tension on a thick substrate, with a corresponding propensity for delamination. Thus the tensile stresses induce a delamination that extends parallel to the surface at a characteristic depth, subject to a steady-state energy release rate [29]. Spallation of coating lamellae could be the consequence of cumulative delamination and material loss caused by sequential cold shocks. The shock requirements for forming surface connected vertical cracks are less stringent than those for forming delaminations. The expectation, therefore, is that vertical cracks develop first [30]. The delamination normally gets extended from the vertical separations. Upon reheating the CMAS fluid would be drawn in by capillarity, filling the delamination. The lamellae, where the CMAS has penetrated, the delaminations are evident in the microstructure as seen in Fig. 13.

4.4.2. *Cross-sectional analysis of LZ duplex coated samples after CMAS attack*

The cross-sectional micrograph of the CMAS attacked LZ duplex specimen is shown in Fig. 14. After 50 CMAS attack cycles, several transverse cracks have propagated and extended inside the LZ coat and most of the cracks are filled with CMAS. It would be susceptible to cause the debonding of the LZ coat from the BC. Further, the CMAS also have penetrated the open porosities and cracks. Open vertical cracks are also in evidence, starting at the surface and extending partially or fully through the CMAS penetrated layer (Fig. 14). These cracks are open and form a characteristic mud-crack pattern at the surface (Fig. 13) typical of thermal stress cracks generated on cooling. Moreover, the cross-sections indicate that the channel cracks initiate and propagate substantially within the CMAS-filled LZ coating. The depth of CMAS penetration is location dependant. In the deeply penetrated regions, multiple sub-surface delaminations are evident as seen in Fig. 14: all originate from the extremity of one of the channels. They are located at three primary levels [31]: (i) just above the bond coat, (ii) adjacent to the bottom of the CMAS penetrated layer and (iii) just below the top surface. Those at level (iii) are filled with CMAS. Level (ii) delaminations often link causing a section of the penetrated material to spall, resulting in a "slab" of ejected material.

Level (i) delaminations are extremely long and especially detrimental to the durability of the TBC. The crack and delamination patterns in Fig. 14 suggest that, where the CMAS has penetrated, tensile stress is developed at the surface on cooling, causing channel cracks to be formed and extended (fully or partially) through the penetrated layer. On further cooling, the energy release rates on the level (ii) become large enough so that delaminations form from the channel cracks and extend adjacent to the CMAS penetrated layer. Thereafter, the energy release rate on the level (i) becomes large enough to extend delaminations from deep channel cracks, just above the bond coat/ TGO layer (in mixed mode). The TGO layer formation is evident at the LZ–BC interface (Fig. 14), but at many locations it has been consumed by the CMAS. Though the CMAS infiltration has played a role in partial failure of LZ duplex coating, the main reasons for the rapid weight gain of LZ coating compared to YSZ coating after twenty three cycles (Fig. 3a) is attributed to the rapid propagation of numerous longitudinal and transverse cracks induced by the thermal shock created in the CMAS cycling experiments. The cross-section of the coating indicates (Fig. 14) extensive cracking and the total integrity of the coating being lost albeit filled with CMAS. The extensive cracking is due to the low fracture toughness (LZ: 1.4 MPa $m^{1/2}$, YSZ: 1.8 MPa $m^{1/2}$) and the low coefficient of expansion (LZ: $9.1 \times 10^{-6}\ K^{-1}$, YSZ: $10.7 \times 10^{-6}\ K^{-1}$) [32].

The low fracture toughness leads to the initiation and growth of micro-cracks even with lower stress levels and the low coefficient of expansion leads to the mismatch in the coefficient of thermal expansion between the top

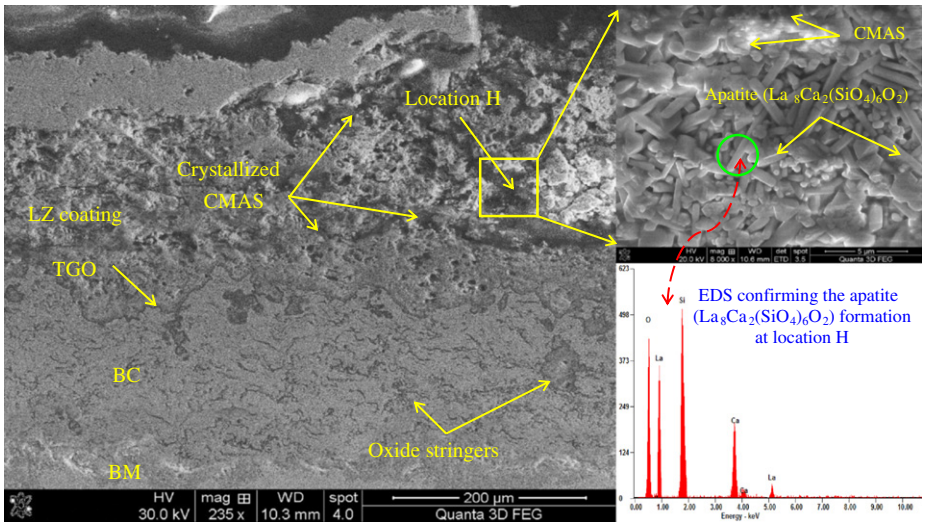

Fig. 14. Cross-sectional image of LZ duplex coating sample exposed to CMAS indicating CMAS infiltration and needle shaped apatite ($La_8Ca_2(SiO_4)_6O_2$) grain formation.

ceramic layer and the BC. This thermal expansion mismatch results in an increase of residual stresses that can cause the failure of coatings even though this coating is comparatively resistant to infiltration by CMAS up to 23 cycles compared to YSZ duplex coating. A higher magnification image taken at the location H of the CMAS infiltrated LZ duplex coating is shown in Fig. 14. In the figure one can see the presence of rod shaped crystals along with crystallized CMAS glass. The EDS pattern taken at location H (Fig. 14) on the rod shaped crystals confirms the existence of elements namely the La, Ca, Si and O, which corresponds to the chemical composition of a lanthanum based apatite ($La_8Ca_2(SiO_4)_6O_2$). The phases present in the LZ coatings before and after CMAS exposure are displayed in Fig. 15. The XRD analysis of the as deposited LZ coating exhibited peaks of a cubic pyrochlore structure as seen in Fig. 15a. Exposure of the coating to molten CMAS resulted in the appearance of peaks (Fig. 15b) attributed to the formation of apatite ($La_8Ca_2(SiO_4)_6O_2$), hexagonal anorthite ($CaAl_2Si_2O_8$), magnesia spinel/orthogonal magnesium aluminate ($MgAl_2O_4$) together with the original LZ cubic pyrochlore peaks. Similarly, The EDS elemental mapping result of the cross-section of the LZ duplex coated specimen is shown in Fig. 16. The Infiltration of CMAS through the cracks and interconnected porosities could be witnessed in the mapping results corresponding to the elements namely Ca, Mg, Al and Si. The CMAS has penetrated through thickness of the LZ coating thereby completely jeopardizing its integrity. The liquid CMAS has also consumed the TGO layer and entered into the bond coat lamellae.

4.5. Interaction between CMAS and five layered coating

The specific weight gain pattern of the sample with five layered coating for 50 cycles of CMAS attack is shown in Fig. 3a. From the figure it could be inferred that the specific weight gain of sample with five layered coating is less compared to all the considered coatings and the BM. The cumulative weight gain (Fig. 3b) of the five layer coated sample comprising of the LZ as top layer is 6 mg/cm^2. The aforementioned evidences indicate the superior CMAS infiltration resistance of the sample provided with the five layered coating.

4.5.1. Surface analysis of five layered coating after CMAS attack

The surface morphology of the five layered coating (Fig. 17) looks similar to that of the LZ duplex coated specimen, but the formation of micro-cracks were largely mitigated due to the gradient nature of the coating (Fig. 17a). The molten CMAS reacted with the top LZ layer and the respective products of reaction were found at certain locations on the surface of the LZ top layer as seen in Fig. 17b. The molten CMAS has infiltrated the top surface of the five layered coating, but the exfoliation of the lamellae has been minimized to a certain extent. The LZ lamellae have reacted with molten CMAS and the reaction products have undergone delamination and chipping, due to the thermal shock, as could be seen in Fig. 17a. Furthermore, cyclic attack by CMAS attack chipped certain lamellae of the LZ top layer and paved way for the intrusion of molten CMAS into the coating. Then the liquid phase CMAS got infiltrated along the grooves and penetrated into pores and cracks within the top LZ layer. During the cooling process, the molten mixture got crystallized from liquid phase and got trapped in the pores and cracks within the top LZ layer of the five layered coating.

4.5.2. Cross-sectional analysis of five layered coating after CMAS attack

The cross-sectional image of the CMAS infiltrated five layered coating is shown in Fig. 18. The coating microstructure in Fig. 18 reveals that CMAS penetrates the splat boundaries of the LZ layer and also has dislodged the

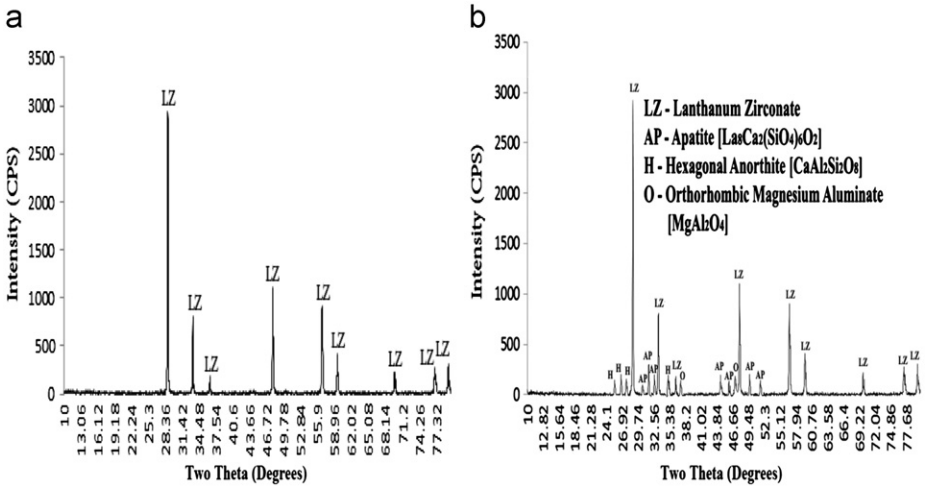

Fig. 15. XRD patterns of LZ coating before and after CMAS test. (a) XRD pattern of as deposited LZ duplex coating. (b) XRD analysis of crushed LZ coat (spalled) after 50 cycles of CMAS attack.

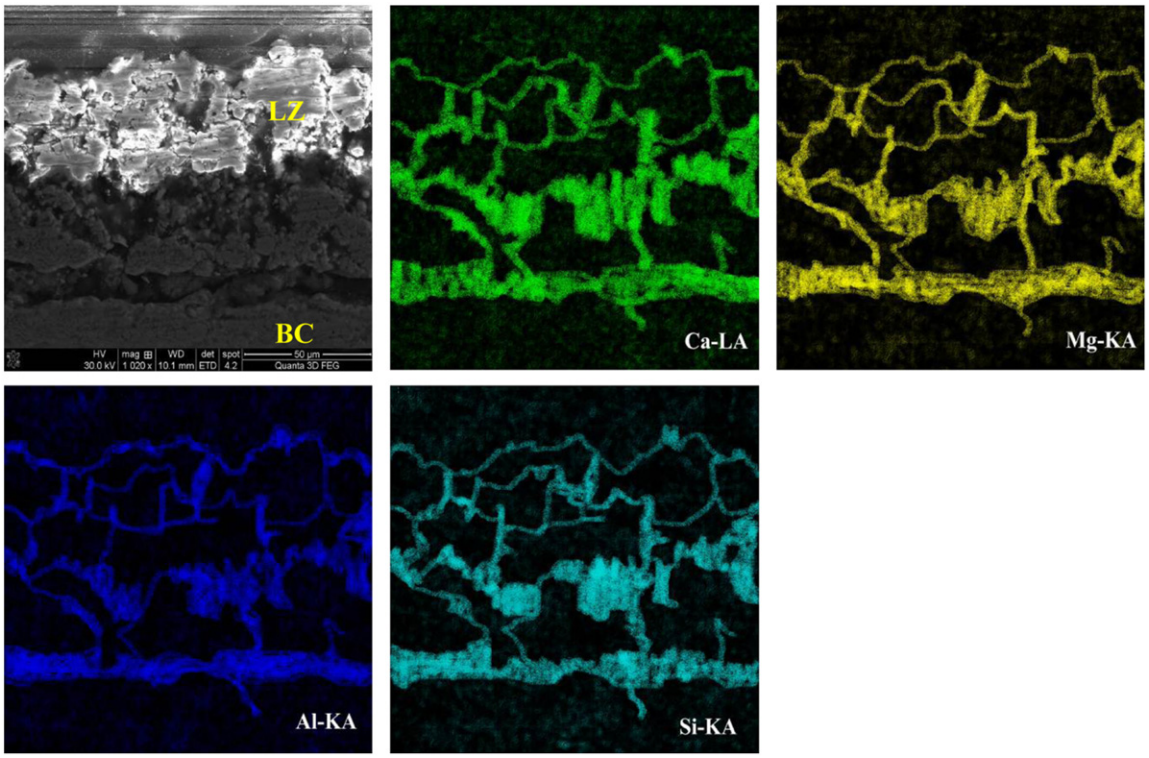

Fig. 16. EDS elemental mapping results of LZ duplex sample exposed to CMAS attack.

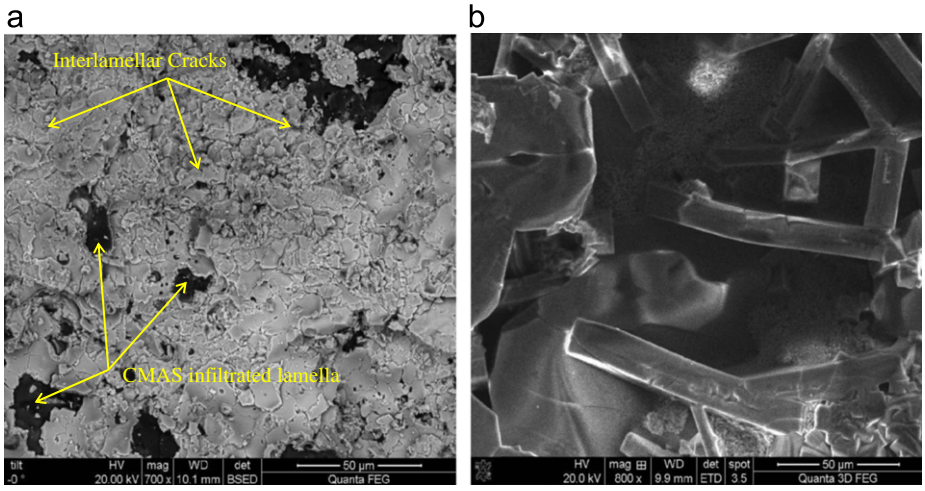

Fig. 17. Images of the top surface of the five layered coating exposed to CMAS taken at different locations. (a) Image of top surface of five layer coated sample exposed to CMAS showing interlamellar cracks and exfoliated lamellae. (b) Image of top surface of five layer coated sample depicting the LZ-CMAS reaction front.

reacted layer crystallites, increasing the area of interaction with the melt. The observation is that the CMAS has penetrated the LZ top layer through the splat boundaries, but the penetration rate, the propensity of CMAS penetration and subsequent cracking of ceramic lamellae has been retarded. The most plausible scenario for the infiltration progressing through the thickness of the coating involves the following order. *Stage I*: when the surface temperature of the five layered coating reaches 1280 °C, the molten fraction of the CMAS deposit penetrates through the cracks of the coating. *Stage II*: because the temperature of the melt decreases with depth into the coating, the viscous drag increases and the penetration rate reduces. Nevertheless, for glasses of this chemistry, the viscosity is sufficiently low so that the penetration can continue well below the isotherm. Indeed, the glass transition temperature of similar glasses ($T_g \approx 800$ °C) implies that a significant layer of under-cooled CMAS is likely to develop within the TBC before the flow becomes sufficiently viscous to fully stop penetration [33]. *Stage III*: crystallization within this under-cooled layer commences (conceivably modified by the reaction taking place between

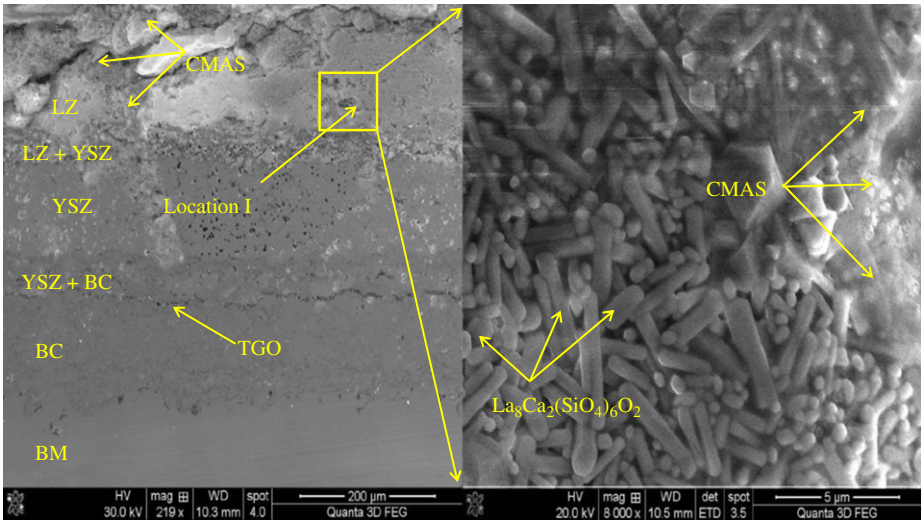

Fig. 18. Cross-sectional image of surface of five layer coated sample indicating CMAS infiltration and needle shaped apatite ($La_8Ca_2(SiO_4)_6O_2$) grain formation.

the molten CMAS and LZ), constricting the infiltration path and eventually blocking the infiltration. The thermochemical interaction between LZ top layer and CMAS is arguably linked to the arrest of the CMAS infiltration, and thus deserves further analysis. The morphology and chemical composition of the crystals found at location I in the five layered coating (Fig. 18) are the same as the ones found in the case of the LZ duplex coated sample. The point mentioned above and the XRD result shown in Fig. 15b confirm the formation of apatite ($La_8Ca_2(SiO_4)_6O_2$), hexagonal anorthite ($CaAl_2Si_2O_8$) and magnesia spinel ($MgAl_2O_4$). In striking contrast to the YSZ and LZ duplex coatings, the five layered coating is intact, with voids and cracks appearing only in the top LZ layer, where the reaction has taken place between the LZ and the molten CMAS.

The reaction layer consists primarily of large acicular needle shaped apatite crystals ($La_8Ca_2(SiO_4)_6O_2$) protruding into the residual anorthite CMAS glass ($CaAl_2Si_2O_8$), interspersed with some globular particles. The crystalline reaction layer thus formed on the top LZ layer is impervious to molten CMAS. The following explanation might be the reason behind the aforementioned effect. Since the La content in LZ is significantly higher than the Y content in YSZ, the dissolution of LZ grains appears to alter greatly the local CMAS composition (La enrichment) relative to the YSZ case. This appears to result in the crystallization of the penetrated molten CMAS, with apatite (Location I in Fig. 18). The apparent inability of apatite to incorporate significant amounts of Mg or Al lead to the super-saturation of these oxides in the melt and their precipitation as anorthite and spinel, the second and third crystalline products of the reaction. Thus, the formation of this impervious, stable crystalline reaction layer prevents the penetration of the molten CMAS to a certain extent. The change in viscosity of the molten CMAS while infiltrating through the coating will also play a major role in the mitigation process. A more likely effect of the thawed species could be on the viscosity of the melt and the ensuing inward flow. There are documented effects of rare-earth additions increasing the viscosity of aluminosilicate glasses [34], but the latter contained no other modifiers like Ca or Mg, and much higher concentrations of rare earth in the melt. Conversely, the crystallization of apatite would increase the Ca:Si ratio in the melt, decreasing its viscosity. Perhaps, the effects of the dissolution of LZ into the CMAS in promoting the crystallization of the melt are more important than those on the melt viscosity. The 50-hour cycling test used in the investigation is of sufficient length to illustrate fully developed molten CMAS attack of TBCs as well as the deceleration of this attack. Also, the peak cycling temperature of 1280 °C used here is typical of TBC surface temperature reached in the next generation aero engine gas-turbines.

Furthermore, the CMAS concentration (35 mg cm^{-2}) used here is sufficiently high to distinguish between complete CMAS penetration in YSZ and LZ duplex coatings and partial penetration in the case of five layered coating with LZ as the top layer. The partial penetration is likely to result in some loss of strain tolerance in the coating relative to the situation without CMAS, but this loss is expected to be significantly lower compared to the complete penetration in the case of YSZ & LZ duplex coated specimens. The LZ top layer impeded the infiltration of the molten CMAS into the underlying YSZ coating. Consequently, destabilization of YSZ was considerably restrained. Additionally, oxidation of the BC was reduced due to the presence of the LZ top layer. The better CMAS resistance of the five layered coated specimen can be regarded as the result of the composition and structure distribution of the gradient region in the coating. It is explained that the thermal stresses arising from the different thermal expansions were greatly relaxed in this kind of gradient coating [35]. This implied that the top LZ

layer impeded the oxidation of the bond coat during cyclic CMAS exposure due to the oxygen non-transparent nature of the LZ material. Further, the crack formation in the top LZ layer of the five layered coating is also greatly mitigated as seen in Fig. 18, which also played a major role in restraining the oxygen diffusion into the coating compared to the LZ duplex and YSZ duplex coatings. The EDS elemental mapping on the cross-section of the five layered coating (Fig. 19) suggests that the molten CMAS concoction was found to react with the top LZ layer and it formed a dense reaction front. There are also evidences of the CMAS which got infiltrated into the five layered coating, but the penetration was largely restricted to the top LZ layer and some minimal permeation can also be seen in the LZ+YSZ intermixed layer of the coating. This indicated that the LZ top layer acted as a barrier against the infiltration of molten CMAS into the YSZ coating.

The thermal stresses can also play a major role in the failure of coatings during cyclic CMAS tests. These stresses can be decreased significantly by employing a gradient coating or by inducting intermixed interfacial layers in the coating [36]. The bond strength can be improved significantly by introducing such intermixed interfacial layers in a coating [37]. The microhardness distributions of the duplex coatings and the five layered coating are displayed in Fig. 2a. It can be observed from the figure that the microhardness changes gradually through the five layered coating, while a significant difference exists for the duplex coatings. The gradual variation of the microhardness of the five layered coatings can reduce the large difference of the elastic modulus between ceramic and metal layers. The increase of bond strength of the five layered coating (Fig. 2b) is also because of the gradual change of the microstructure without sharp interface between different layers. The high bond strength and the gradual variation of the microhardness between the top ceramic coating and the substrate are beneficial to maintain the coating integrity (alleviation of cracks) under the strain generated by the alternating compressive and tensile stresses generated during the cyclic CMAS attack test. Compared with the other considered coatings, the gradient coating improved the CMAS infiltration resistance in the 50-hour cycling test. Therefore, it can be summarized that the resistance of the gradient coating to cyclic CMAS attack is superior to that of the traditional two-layered YSZ (duplex) coating. The last failure step of the five layered coating may be accomplished firstly by delamination of the CMAS infiltrated layer containing the crystallized reaction products. Furthermore, if continuously in service, the coating experiences gradual loss of material from the surface and or spallation near the LZ top coat/ LZ+YSZ interface. The spallation may be attributed to the thermal expansion mismatch between the solidified reaction layer and the LZ layer. It was found that in the case of the five layered coating, in spite of the partial spallation of LZ top layer and the infiltration of CMAS into the intermixed LZ+YSZ layer, the third layer from the top i.e., the YSZ layer remained almost unattacked (Fig. 18). As a result, the five layered coating, with LZ top layer can interact not only with CMAS deposits, but also other types of deposits (salts, ash, and contaminants), and lessen their attack on TBCs.

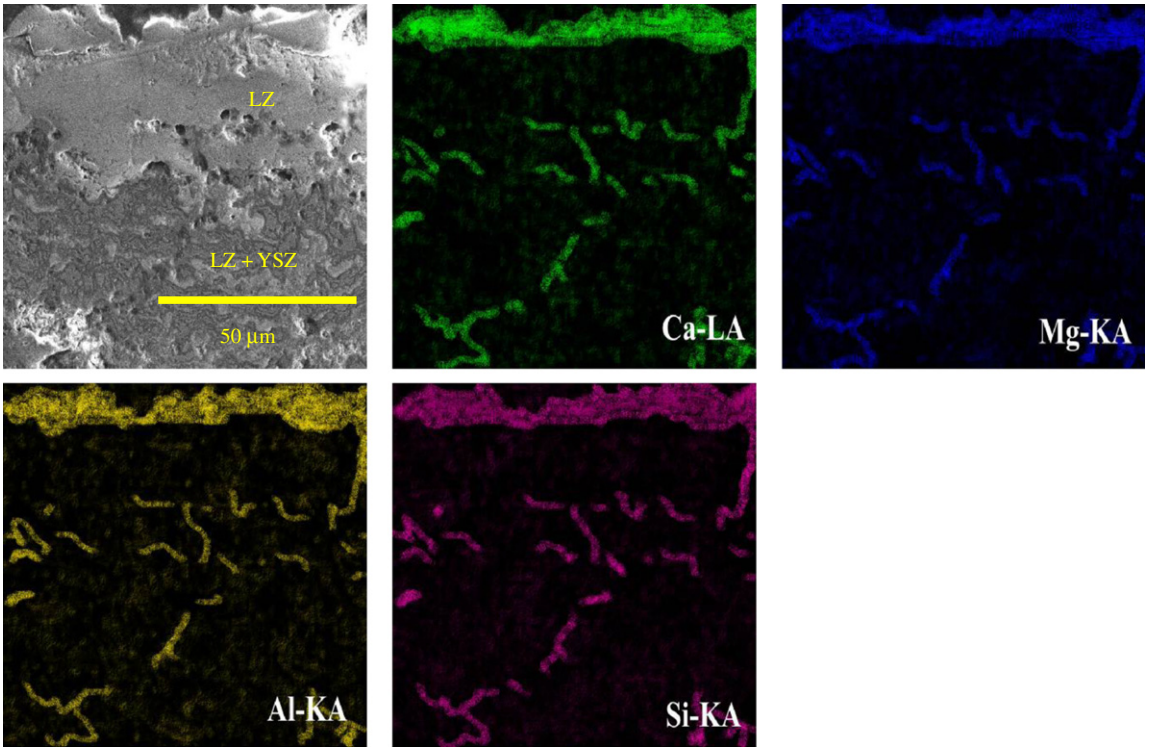

Fig. 19. EDS elemental mapping results of top two layers of the five layered coated sample exposed to CMAS attack.

5. Conclusions

The state of the art YSZ duplex, the LZ duplex and the five layered coatings were fabricated by the APS process and the cyclic CMAS infiltration behaviour of these coatings were systematically investigated and compared with those of the HVOF sprayed NiCrAlY bond coat (BC) and the bare Inconel 738 substrate (BM) coupons. The conclusions that were attained are put forth as follows:

- The bare Inconel 738 substrate (BM) coupons showed considerable weight gain during cyclic CMAS attack due to the infiltration of the molten CMAS though the grain boundaries. The grains underwent severe oxidation and formed complex spinels. These spinels $(Ni,Co)(Al,Cr)_2O_4$ imposed severe strain in the oxidized scale leading to its extensive spallation.
- The HVOF sprayed NiCrAlY coating (BC) improved the infiltration resistance of the BM in the given conditions. The molten CMAS consumed the thermally grown oxide (TGO), alpha-Al_2O_3 during the test. The CMAS glass got enriched with Al content and formed the anorthite phase along with complex spinels. The anorthite $CaAl_2Si_2O_8$ glass composition which is easier-to-crystallize prevented the molten glass from infiltrating deep into the BC; hence the oxidative weight gain of BC was comparably lesser than that of the BM.
- Molten CMAS was found to melt and infiltrate the porous YSZ coating. CMAS infiltration in the YSZ coating resulted in the dissolution of the YSZ followed by the reprecipitation of globular ZrO_2 grains with different polymorphs and composition based on the local melt chemistry. The disruptive phase transformation of t′ to t+m and t to m+c occurred. This phase transformation is attributed to the deviation in the content of Y_2O_3 stabilizer from the original YSZ solid solution during reprecipitation.
- The CMAS infiltration did play a role in the partial failure of LZ duplex coating. The main reasons for the rapid weight gain of LZ duplex coating compared to that of the YSZ coating after 23 cycles, is attributed to the rapid propagation of numerous longitudinal and transverse cracks, induced by the thermal shock created in the CMAS cycling experiments.
- Exposure of the LZ duplex coating to molten CMAS resulted in the formation of apatite $(La_8Ca_2(SiO_4)_6O_2)$, hexagonal anorthite $(CaAl_2Si_2O_8)$, magnesia spinel/ orthogonal magnesium aluminate $(MgAl_2O_4)$ together with the original LZ cubic pyrochlore peaks. Though the formation of the aforementioned phases should have mitigated the CMAS infiltration, the intrinsic low coefficient of expansion and the low fracture toughness of LZ lead to the formation of numerous cracks through which the oxidation took place and eventually increased the weight gain of the sample, compared to YSZ.
- In the case of the five layered coating, the presence of a LZ top layer reduced the infiltration of molten CMAS into the YSZ coating, which refrained the structural destabilization of the inner YSZ. The LZ top layer developed a reaction layer made of needle shaped acicular apatite $(La_8Ca_2(SiO_4)_6O_2)$, hexagonal anorthite $(CaAl_2Si_2O_8)$ and magnesia spinel $(MgAl_2O_4)$ during exposure to the molten CMAS concoction. The lanthanum base apatite got crystallized inside the infiltrated cracks and prevented further infiltration, thereby reducing the oxidation rate of the five layered TBC.
- The gradual change in the microhardness distribution and the high adhesion strength provided a large reduction in stress and stress gradient that formed during high temperature cyclic CMAS attack on the five layered coating. The mitigation the crack formation due to the gradient nature of the layers prolonged the lifetime of the five layered coating.
- The developed five layered coating can be successfully applied on aero engine turbines to increase their efficiency and to mitigate the molten CMAS infiltration.

Acknowledgement

The corresponding author wishes to express his sincere thanks to the Department of Science and Technology (DST), Government of India, New Delhi for the fellowship and the financial support to carry out this investigation through sponsored fast track scheme for young scientists R&D project no. SR/FT/ETA-01/2009.

References

[1] Tom Strangman, Derek Raybould, Ahsan Jameel, Wil Baker, Damage mechanisms, life prediction, and development of EB-PVD thermal barrier coatings for turbine airfoils, Surface and Coatings Technology 202 (2007) 658–664.
[2] M. Wen, E. Jordan, M. Gell, Effect of temperature on rumpling and thermally grown oxide stress in an EB-PVD thermal barrier coating, Surface and Coatings Technology 201 (2006) 3289–3298.
[3] A.G. Evans, D.R. Mumm, J.W. Hutchinson, G.H. Meier, F.S. Pettit, Mechanisms controlling the durability of thermal barrier coatings, Progress in Materials Science 46 (2001) 505–553.
[4] R.G. Wellman, J.R. Nicholls, Erosion, corrosion and erosion–corrosion of EB PVD thermal barrier coatings, Tribology International 41 (2008) 657–662.
[5] Andrew D. Gledhill, Kongara M. Reddy, Julie M. Drexler, Kentaro Shinoda, Sanjay Sampath, Nitin P. Padture, Mitigation of damage from molten fly ash to air-plasma-sprayed thermal barrier coatings, Materials Science and Engineering A 528 (2011) 7214–7221.
[6] G. Witz, V. Shklover, W. Steurer, S. Bachegowda, H.P. Bossmann, High-temperature interaction of yttria stabilized zirconia coatings with CaO–MgO–Al_2O_3–SiO_2 (CMAS) deposits, http://dx.doi.org/10.1016/j.surfcoat.2009.07.034.
[7] B. Saruhan, P. Francois, K. Fritscher, U. Schulz, EB-PVD processing of pyrochlore-structured $La_2Zr_2O_7$-based TBCs, Surface and Coatings Technology 182 (2004) 175–183.
[8] R. Vaßen, M.O. Jarligo, T. Steinke, D.E. Mack, D. Stöver, Overview on advanced thermal barrier coatings, Surface and Coatings Technology 205 (2010) 938–942.
[9] C.S. Ramachandran, V. Balasubramanian, P.V. Ananthapadmanabhan, V. Viswabaskaran, Influence of the intermixed interfacial layers on the

thermal cycling behaviour of atmospheric plasma sprayed lanthanum zirconate based coatings, Ceramics International 38 (2012) 4081–4096.
[10] C.S. Ramachandran, V. Balasubramanian, P.V. Ananthapadmanabhan, Synthesis, spheroidization and spray deposition of lanthanum zirconate using thermal plasma process, Surface and Coatings Technology 206 (2012) 3017–3035.
[11] C.S. Ramachandran, V. Balasubramanian, P.V. Ananthapadmanabhan, Optimization of atmospheric plasma spray process parameters to deposit yttria-stabilized zirconia coatings using response surface methodology, Journal of Thermal Spray Technology 20 (2011) 590–607.
[12] Kramer Stephan, James Yang, Carlos G. Levi, Infiltration-inhibiting reaction of gadolinium zirconate thermal barrier coatings with CMAS melts, Journal of the American Ceramic Society 91 (2008) 576–583.
[13] Taniguchi Shigeji, Toshio Maruyama, Masayuki Yoshiba, Nobuo Otsuka, Yuuzou Kawahara, Advanced coatings on high temperature applications, Materials Science Forum 522–523 (2006) 1–14.
[14] S.M. Jiang, H.Q. Li, J. Ma, C.Z. Xu, J. Gong, C. Sun, High temperature corrosion behaviour of a gradient NiCoCrAlYSi coating II: oxidation and hot corrosion, Corrosion Science 52 (2010) 2316–2322.
[15] R.A. Mahesh, R. Jayaganthan, S. Prakash, Evaluation of hot corrosion behaviour of HVOF sprayed NiCrAl coating on superalloys at 900 °C, Materials Chemistry and Physics 111 (2008) 524–533.
[16] N. Eliaz, G. Shemesh, R.M. Latanision, Hot corrosion in gas turbine components, Engineering Failure Analysis 9 (2002) 31–43.
[17] Aygun Aysegul, Alexander L. Vasiliev, Nitin P. Padture, Xinqing Ma, Novel thermal barrier coatings that are resistant to high-temperature attack by glassy deposits, Acta Materialia 55 (2007) 6734–6745.
[18] E.M. Levin, C.R. Robbins, H.F. McMurdie, Phase Diagrams for Ceramists, vol. I, The American Ceramic Society, Columbus (OH), 1964.
[19] P. Mohan, B. Yuan, T. Patterson, V.H. Desai, Y.H. Sohn, Degradation of yttria stabilized zirconia thermal barrier coatings by molten CMAS (CaO-MgO-Al_2O_3-SiO_2) deposits, Materials Science Forum 595–598 (2008) 207–212.
[20] T.M. Shaw, P.R. Duncombe, Forces between aluminum oxide grains in a silicate melt and their effect on grain boundary wetting, Journal of the American Ceramic Society 74 (1991) 2495–2505.
[21] Julie M. Drexler, Kentaro Shinoda, Angel L. Ortiz, Dongsheng Li, Alexander L. Vasiliev, Andrew D. Gledhill, Sanjay Sampath, Nitin P. Padture, Air-plasma-sprayed thermal barrier coatings that are resistant to high-temperature attack by glassy deposits, Acta Materialia 58 (2010) 6835–6844.
[22] Travis Prabhakar Mohan, Bo Patterson, Yongho Yao, Sohn, Degradation of thermal barrier coatings by fuel impurities and CMAS: Thermochemical interactions and mitigation approaches, Journal of Thermal Spray Technology 19 (2010) 156–167.
[23] Wolfgang Braue, Environmental stability of the YSZ layer and the YSZ/TGO interface of an in-service EB-PVD coated high-pressure turbine blade, Journal of Materials Science 44 (2009) 1664–1675.
[24] Wu Jing, Hong-bo Guo, Yu-zhi Gao, Sheng-kai Gong, Microstructure and thermo-physical properties of yttria stabilized zirconia coatings with CMAS deposits, Journal of the European Ceramic Society 31 (2011) 1881–1888.
[25] H.B. Guo, H. Murakami, S. Kuroda, Effects of heat treatment on microstructures and physical properties of segmented thermal barrier coatings, Materials Transactions 46 (2005) 1775–1778.
[26] R. Vaßen, N. Czech, W. Malléner, W. Stamm, D. Stöver, Influence of impurity content and porosity of plasma-sprayed yttria-stabilized zirconia layers on the sintering behaviour, Surface and Coatings Technology 141 (2001) 135–140.
[27] S. Tekeli, M. Gürü, Microstructural design and high temperature tensile deformation behaviour of 8 mol% yttria stabilized cubic zirconia (8YCSZ) with SiO_2 additions, Ceramics International 34 (2008) 137–140.
[28] S. Kramer, S. Faulhaber, M. Chambers, D.R. Clarke, C.G. Levi, J.W. Hutchinson, A.G. Evans, Mechanisms of cracking and delamination within thick thermal barrier systems in aero-engines subject to calcium–magnesium-alumino-silicate (CMAS) penetration, Materials Science and Engineering A 490 (2008) 26–35.
[29] C. Mercer, S. Faulhaber, A.G. Evans, R. Darolia, A delamination mechanism for thermal barrier coatings subject to calcium–magnesium-alumino-silicate (CMAS) infiltration, Acta Materialia 53 (2005) 1029–1039.
[30] L.G. Zhao, T.J. Lu, N.A. Fleck, Crack channelling and spalling in a plate due to thermal shock loading, Journal of the Mechanics and Physics of Solids 48 (2000) 867–897.
[31] A.G. Evans, J.W. Hutchinson, The mechanics of coating delamination in thermal gradients, Surface and Coatings Technology 201 (2007) 7905–7916.
[32] T. Ohji, T. Sekino, K. Niihara, Thermal evolution of single phase lanthanum zirconate, Key Engineering Materials 317 (2006) 31–36.
[33] D. Giordano, D.B. Dingwell, The kinetic fragility of natural silicate melts, Journal of Physics: Condensed Matter 15 (2003) S945–S954.
[34] P.F. Becher, M.K. Ferber, Temperature-dependent viscosity of Si RE Al-based glasses as a function of N: O and RE: Al ratios (RE = La, Gd, Y, and Lu), Journal of the American Ceramic Society 87 (2004) 1274–1279.
[35] Huibin Xu, Hongbo Guo, Fushun Liu, Shengkai Gong, Development of gradient thermal barrier coatings and their hot-fatigue behaviour, Surface and Coatings Technology 130 (2000) 133–139.
[36] Hongbo Guo, Shengkai Gong, Huibin Xu, Evaluation of hot-fatigue behaviors of EB-PVD gradient thermal barrier coatings, Materials Science and Engineering A 325 (2002) 261–269.
[37] C. Giolli, A. Scrivani, G. Rizzi, F. Borgioli, G. Bolelli, L. Lusvarghi, Failure mechanism for thermal fatigue of thermal barrier coating systems, Journal of Thermal Spray Technology 18 (2009) 223–230.